



Shape-controlled nanostructured magnetite-type materials as highly efficient Fenton catalysts



Liwei Hou^a, Qinghua Zhang^b, François Jérôme^b, Daniel Duprez^b, Hui Zhang^{a,**}, Sébastien Royer^{b,*}

^a Department of Environmental Engineering, Wuhan University, P.O. Box C319, Luoyu Road, 129#, Wuhan 430079, PR China

^b Université de Poitiers, CNRS UMR 7285, IC2MP, 4 rue Michel Brunet, 86022 Poitiers Cedex, France

ARTICLE INFO

Article history:

Received 5 April 2013

Received in revised form 22 July 2013

Accepted 31 July 2013

Available online 11 August 2013

Keywords:

Fe₃O₄

Ionic liquid

Porous materials

Iron phase

Fenton

ABSTRACT

Nanostructured Fe₃O₄ particles were obtained through hydrogen thermal reduction of α-Fe₂O₃ particles synthesized via an ionic liquid assisted hydrothermal process. The morphology and microstructure of the nano-sized Fe₃O₄ particles were characterized by using X-ray diffraction, N₂ physisorption, transmission electron microscopy, and temperature-programmed reduction. As-prepared magnetite samples show microcube, nanosphere, and porous nanorod morphologies. Activity of the nanostructures was evaluated for the Fenton reaction, using phenol as model molecule. While commercial Fe₃O₄ presents very limited activity, rod-type nanostructure exhibited exceptional activity toward phenol removal under mild conditions; 98% phenol was converted, and the total organic carbon (TOC) abatement was 74%. The reusability of porous nanorods of Fe₃O₄ was also investigated after three successive runs, which demonstrated the promising application of the catalyst in the oxidative degradation of organic pollutants. In addition, the material activity is strongly affected by the reduction degree, highlighting the beneficial effect of Fe⁰/Fe₃O₄ mixed phase formation to achieve higher activity.

© 2013 Elsevier B.V. All rights reserved.

1. Introduction

Iron oxides are transition metal oxides, natural minerals and geocatalysts, existing in the natural aqueous environment, and also suspending in aerosol, clouds, and fogs as fine particles [1,2]. Because iron oxides are inexpensive and relatively non-toxic in comparison to other transition metals (including nickel, chromium, copper), they are preferred for the extensive application in many fields, such as corrosion processes [3,4], electromagnetic devices [5], and catalytic reactions [6–9]. The versatility of the surface composition among Fe⁰, Fe^{II} and Fe^{III} over different types of iron oxides (Fe⁰, FeO, α-Fe₂O₃, γ-Fe₂O₃, Fe₃O₄, α-FeOOH, β-FeOOH, γ-FeOOH and δ-FeOOH) ensure tunable properties, conferring to some composition high activity for heterogeneous Fenton reactions at the catalyst/solution interface [10]. Significantly different catalytic activities are then observed to be dependant on the material crystallographic and surface properties, due to variable valences of iron that can be stabilized [10].

More recently, several environmental applications of iron compounds (e.g., as reducing agents and as promoters in the Fenton

reaction) have been intensively investigated [11]. For example, Fe⁰ has been proposed as a low-cost and nontoxic material in environmental remediation processes [12,13]. Different iron compounds, such as Fe⁰, Fe₃O₄ [14] and Fe⁰/Fe₃O₄ [15] have been reported to promote the Fenton reaction. Although the kinetic of these processes is highly complex and dependent on numerous different parameters, an important rate-limiting step is the production of radicals. In this respect, the exposed site valence on the iron surface and the presence of oxide/hydroxide layers that cover the iron particles should strongly influence the rate of the process [16]. The development of new processes to increase iron oxide efficiencies and to widen the application of these systems in environmental remediation processes is of great interest.

Magnetite (Fe₃O₄)-based heterogeneous systems have attracted attention due to their unique properties and their potential applications in numerous fields, including ferrofluids, targeted drug delivery, and water treatment [17–20]. Especially, magnetite has also been reported to be an efficient catalyst for Fenton-like processes [21–31]. Magnetite exhibits several features that are important for a Fenton reaction: (i) it contains Fe²⁺ that might play an important role as an electron donor to initiate the Fenton reaction; (ii) the octahedral site in the magnetite structure can easily accommodate both Fe²⁺ and Fe³⁺, which means that Fe²⁺ can be reversibly oxidized and reduced in the same structure; and (iii) Fe₃O₄ has peroxidase-like activity and can activate H₂O₂ [14]. In addition, recent works demonstrated that bringing Fe⁰ particles

* Corresponding author. Tel.: +33 0 549453479; fax: +33 0 549453499.

** Corresponding author. Tel.: +86 0 27 68775837; fax: +86 0 27 68778893.

E-mail addresses: eeng@whu.edu.cn (H. Zhang), sebastien.royer@univ-poitiers.fr (S. Royer).

into contact with Fe_3O_4 particles through grinding increases the activity of magnetite for H_2O_2 decomposition [15,32]. Thus, activity in the Fenton reaction was improved over these mixed phase materials.

As far, a wide variety of method has been reported to synthesize Fe_3O_4 nanoparticles, including sol–gel methods [33], wet-chemical methods [34], hydrothermal methods [35], and co-precipitation [36]. However, these methods tend to form Fe_3O_4 particles with isotropic shapes. Nevertheless, various Fe_3O_4 nanostructures with different morphologies have been successfully synthesized, including nanotubes, nanowires, nanofilms, spheres, nanorods, and other novel structures using routes such as coprecipitation, microemulsion, and so on [37–39].

Recently, reduction of premade isotropic $\beta\text{-FeOOH}$ or $\alpha\text{-Fe}_2\text{O}_3$ particles into Fe_3O_4 was proposed [40–42]. Compared with other methods, reduction of premade $\alpha\text{-Fe}_2\text{O}_3$ is a simple and effective method. Generally, the reduction of $\alpha\text{-Fe}_2\text{O}_3$ involves an annealing process under reductive atmosphere at moderate temperature (about 300–500 °C). However, the annealing treatment of the premade materials may result in undesirable aggregation and sintering. Since the shape of formed Fe_3O_4 particles is dependent on that of premade $\alpha\text{-Fe}_2\text{O}_3$, it is important to achieve $\alpha\text{-Fe}_2\text{O}_3$ synthesis with various shapes prior to the reduction process. As reported in our previous work [43], ionic liquids (ILs) assisted hydrothermal route is found to be an effective method to synthesize $\alpha\text{-Fe}_2\text{O}_3$ nanoparticles of various shapes, such as cubes, nanorods as well as nanoplates. Compared with the traditional hydrothermal methods, high surface area can be achieved due to reduction in crystal size by employing the ILs as the soft template. Because the properties of nanomaterials are influenced by their structure, size, and shape [37], the preparation of Fe_3O_4 nanoparticles with different sizes and morphologies is an important issue.

Herein, we report an environmentally benign “green” route to the synthesis of Fe_3O_4 nanoparticles with various morphologies, achieved by reduction of pre-made $\alpha\text{-Fe}_2\text{O}_3$ materials. The physical and chemical characterization of Fe_3O_4 was performed, and the effect of the morphology and crystal structure of Fe_3O_4 on the catalytic wet peroxide oxidation process was investigated. Because of their unique porous structure, the potential applicability of nanorods of Fe_3O_4 in heterogeneous Fenton reactions was evaluated with respect to changes in the catalyst and the H_2O_2 concentrations, as well as with respect to the material's stability. Further activity improvement was achieved optimizing the $\text{Fe}^0/\text{Fe}_3\text{O}_4$ balance through reduction temperature.

2. Experimental

2.1. Materials

All chemicals employed in the preparation of the $\alpha\text{-Fe}_2\text{O}_3$ in ionic liquid media and derived Fe_3O_4 catalysts were used as purchased: 1-methylimidazole ($\text{C}_4\text{H}_6\text{N}_2$, $\geq 99\%$, Sigma-Aldrich), 1-Chlorodecane [$(\text{CH}_3(\text{CH}_2)_9\text{Cl}$, 98%, Sigma-Aldrich], ethyl acetate ($\text{CH}_3\text{COOC}_2\text{H}_5$, 99.8%, Sigma-Aldrich), $\text{FeCl}_3 \cdot 6\text{H}_2\text{O}$ ($\geq 98\%$, Sigma-Aldrich), potassium acetate (CH_3COOK , $\geq 99\%$, Sigma-Aldrich), and sodium hydroxide (NaOH , $\geq 98\%$, Sigma-Aldrich). For the heterogeneous Fenton reaction, phenol ($\text{C}_6\text{H}_5\text{OH}$, $\geq 99\%$, Sigma-Aldrich) and hydrogen peroxide solution (H_2O_2 , 32 wt.% in H_2O , Sigma-Aldrich) were used as received. The ionic liquid ($\text{C}_{10}\text{mimCl}$) used here was synthesized and used to prepare three kinds of $\alpha\text{-Fe}_2\text{O}_3$ with different morphologies via the hydrothermal method (see details in SI, Materials). $\text{Fe}_3\text{O}_4\text{-M}$ catalysts, where M represents the morphology of the catalyst, were obtained through the reduction of the $\alpha\text{-Fe}_2\text{O}_3$ under H_2 at a flow rate of 60 mL min^{-1} at 300 °C for 1 h. The samples were denoted $\text{Fe}_3\text{O}_4\text{-C}$ (‘C’ for microcube), $\text{Fe}_3\text{O}_4\text{-S}$ (‘S’ for microsphere), and $\text{Fe}_3\text{O}_4\text{-R}$ (‘R’ for nano-rods).

2.2. Catalysts characterization

The $\alpha\text{-Fe}_2\text{O}_3$ and Fe_3O_4 catalysts were systematically characterized using X-ray diffraction (XRD), N_2 physisorption, transmission electron microscopy (TEM), ICP-OES, and temperature-programmed reduction (TPR).

The catalyst structures were verified by X-ray diffraction using a D5005 diffractometer from Bruker equipped with a $\text{Cu K}\alpha$ radiation ($\lambda = 1.5406\text{ \AA}$) source. The signal was recorded for 2θ between 20° and 80° with a recording step of 0.05° every 3 s. Phase identification was made through comparison with the JCPDS database. The crystallite sizes were determined using the Scherrer equation after Warren's correction for instrumental broadening was applied. (1 1 3) reflection was used for calculation of Fe_2O_3 crystal size, while (3 1 1) reflection was used in the case of Fe_3O_4 phase.

The N_2 adsorption measurements were performed on a Micromeritics TRISTAR 3000 instrument. The specific surface area of the catalysts was measured at liquid N_2 temperature (−196 °C), using the Brunauer–Emmett–Teller (BET) method. Prior to analysis, sample was heated under vacuum at 250 °C for 3 h.

The material morphologies were evaluated by transmission electron microscopy (TEM) coupled with energy-dispersive X-ray spectroscopy (EDXS). Micrographs were obtained on a JEOL 2100 instrument (operated at 200 kV with a LaB_6 source and equipped with a Gatan Ultrascan camera).

TPR experiments were performed on an AUTOCHEM instrument from Micromeritics. Approximately 50 mg of sample was introduced into the microreactor. The material was initially activated under simulated air (total flow rate = 30 mL min^{-1}) at 300 °C for 1 h. After the sample was cooled to room temperature, a reducing flow (1 vol.% of H_2 in Ar) was stabilized at a flow rate of 30 mL min^{-1} , and the temperature of the reactor was subsequently increased from 50 °C to 1000 °C with a ramp of 5 °C min^{-1} . The change in the H_2 concentration as a function of temperature was recorded using an online TCD.

The total Fe^{2+} content in the bulk of Fe_3O_4 was determined by chemical analysis after the samples were dissolved in acidic media at 60 °C for 48 h under a nitrogen atmosphere. According to Xue et al. [9], 6 mol L^{-1} HCl was used to ensure the dissolution of the catalysts. 1.0 mL of 1,10-phenanthroline (1.0 g L^{-1}) was then added to the dissolved sample to form a colored complex. Finally, complex concentration was measured by UV spectrophotometer at λ fixed at 510 nm [44].

Furthermore, the surface ratio of $\text{Fe}^{\text{II}}/\text{Fe}^{\text{III}}$ on the Fe_3O_4 surface was also analyzed by X-ray Photoelectron Spectroscopy (XPS). Analyses were conducted on a Thermo-Fisher ESCALAB 250 system with $\text{Al K}\alpha$ radiation under ultrahigh vacuum (UHV). Binding energies were calibrated with the $\text{C}1\text{s}$ binding energy fixed at 285 eV as internal reference. Curve fittings were achieved with the XPS Peak software using the $\text{Fe}2\text{p}$ binding energies region for the analysis.

2.3. Catalytic activity measurement

Catalytic tests were performed under mild conditions (atmospheric pressure and 25 °C) in a 150 mL glass reactor continuously stirred using phenol as reactant and hydrogen peroxide as oxidant. We initially verified that no external or internal diffusional resistances occurred and that the reaction was performed in a kinetic regime. The reaction pH value was adjusted to 4.0 before the oxidation began. In a typical experiment, 100 mL of phenol aqueous solution was prepared with an initial concentration of 600 mg L^{-1} . The catalyst was subsequently added to the solution, which was then stirred in the dark until the adsorption–desorption equilibrium was obtained prior to initiation of oxidation. At the end of this step, we obtain the C_0 concentration. Then, the H_2O_2 solution was added dropwise at a constant rate to the solution

during the 5 first minutes of the reaction. The initial reaction time, t_0 , is defined at the starting of the H_2O_2 adding. The reaction solution was sampled at fixed time intervals and half of the solution is mixed with 0.1 g of manganese oxide for at least 15 min to eliminate residual H_2O_2 . The reaction solution was then filtered through a 0.22 μm membrane before the residual phenol concentration and the total organic carbon (TOC) were measured. The calculation of phenol conversion was performed, taking into account the initial adsorption on the material surface (Eq. (1)):

$$X_{\text{phenol}} = \frac{C_t}{C_0} \times 100\% \quad (1)$$

where C_t is the phenol concentration at time t (min) and C_0 is the initial phenol concentration after stabilization due to the adsorption on the catalyst surface.

The calculation of TOC abatement was also performed, taking into account the initial adsorption on the material surface (Eq. (2)):

$$X_{\text{TOC}} = \frac{C_{\text{TOC}}}{C_{\text{TOC}_0}} \times 100\% \quad (2)$$

where C_{TOC} is the TOC concentration at time t (min) and C_{TOC_0} is the initial TOC concentration after stabilization due to the adsorption on the catalyst surface.

Methods: The phenol concentration was determined using a high-performance liquid chromatography (HPLC) instrument equipped with an Aminex HPX-87 (BioRad) column. TOC content was measured using a 1020A Bioritech TOC meter. The concentration of H_2O_2 after the reaction tests was measured via colorimetry using a UV spectrophotometer (Secomam, RS232) after complexation of the hydrogen peroxide with a vanadate salt.

At the end of the catalytic test, the dissolved ferrous iron concentration was also measured via the 1,10-phenanthroline method at 510 nm [44], while the total aqueous iron leaching into the solution was systematically evaluated by inductively coupled plasma optical emission spectroscopy (ICP-OES) analyses through quantification of the dissolved iron concentration in the solution after the tests.

3. Results and discussions

3.1. Characterization of the $\alpha\text{-Fe}_2\text{O}_3$ precursors

The final properties of the active Fe_3O_4 materials are conditioned by the properties displayed by the $\alpha\text{-Fe}_2\text{O}_3$ precursors. Consequently, structural and textural properties of the precursors, as well as their reducibility, are presented thereafter.

3.1.1. X-ray diffraction results

The $\alpha\text{-Fe}_2\text{O}_3$ precursors with different morphologies were prepared using a hydrothermal method. The purity and crystallinity of the as-prepared samples were examined using powder XRD measurements. Fig. 1 displays the XRD patterns of the as-prepared $\alpha\text{-Fe}_2\text{O}_3$ microcubes ($\text{Fe}_2\text{O}_3\text{-C}$), microspheres ($\text{Fe}_2\text{O}_3\text{-S}$), and nanorods ($\text{Fe}_2\text{O}_3\text{-R}$, prepared by annealing of the as-prepared $\alpha\text{-FeOOH}$ nanorods in air at 300°C for 3 h). All the peaks could be indexed to the hexagonal structure of $\alpha\text{-Fe}_2\text{O}_3$, which was in good agreement with literature results (JCPDS Card 33-0664). No other peaks were observed, which indicated the high purity of the prepared samples. The diffraction peaks located at $2\theta = 24.3, 33.3, 35.7, 41.1, 49.7, 54.1, 62.5$ and 64.1° could be indexed to the (0 1 2), (1 0 4), (1 1 0), (1 1 3), (0 2 4), (1 1 6), (2 1 4) and (3 0 0) planes of $\alpha\text{-Fe}_2\text{O}_3$, respectively. However, the differences among the full-width at half-maximum (FWHM) and relative intensities of the diffraction peaks indicated differences in the crystal sizes and morphologies of the particles. The narrow, sharp peaks obtained for

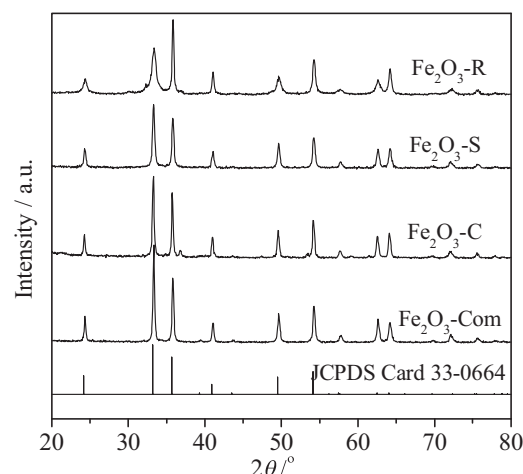


Fig. 1. XRD patterns recorded for different morphologies of $\alpha\text{-Fe}_2\text{O}_3$ precursor.

the commercial $\alpha\text{-Fe}_2\text{O}_3$ ($\text{Fe}_2\text{O}_3\text{-Com}$) and $\text{Fe}_2\text{O}_3\text{-C}$ indicated that these materials presented large crystal sizes. However, the peaks obtained for $\text{Fe}_2\text{O}_3\text{-S}$ were broadened with decreased intensities, which suggested that the crystal size of this sample was smaller than that of Fe-C and Fe-Com . The $\text{Fe}_2\text{O}_3\text{-R}$ sample exhibited the broadest reflections, which suggested that this material exhibited the smallest crystal size among the investigated samples. According to the FWHM evolution, the average crystallite sizes of the $\text{Fe}_2\text{O}_3\text{-C}$, $\text{Fe}_2\text{O}_3\text{-S}$, and $\text{Fe}_2\text{O}_3\text{-R}$ were estimated to be 38, 34, and 24 nm, respectively (Table 1). For comparison, the average crystal size of the commercial $\alpha\text{-Fe}_2\text{O}_3$ (Fe-Com) was 49 nm.

3.1.2. Evolution of physical properties

As shown in Table 1, all the nanostructured materials exhibited greater surface areas than the commercial material. With different morphologies of $\alpha\text{-Fe}_2\text{O}_3$, different surface areas were obtained. Indeed, relatively low surface area of $3.4\text{ m}^2\text{ g}^{-1}$ was obtained for $\text{Fe}_2\text{O}_3\text{-C}$. The sphere morphology led to a greater surface area ($12.3\text{ m}^2\text{ g}^{-1}$), and, for the nanorod-like material, the surface area was $46.5\text{ m}^2\text{ g}^{-1}$. As evident from the results in Table 1, the surface area depended on the crystal size evaluated by X-ray line broadening. The evolution of the surface area with crystal size over the IL-mediated materials showed an exponential decrease with increasing crystal size. Compared with the classical material, the ILs-derived materials showed great enhancement in physical properties (morphology, crystal size, surface area, and density), indicating that the ionic liquid not only affected the morphologies of the materials, but also affected the porosity or density of the formed aggregates. Due to a higher surface area, the nanorod-like material ($\text{Fe}_2\text{O}_3\text{-R}$) is believed to favor the adsorption/reaction of organic pollutants in water-treatment applications.

3.1.3. Morphology of $\alpha\text{-Fe}_2\text{O}_3$

TEM images of the four materials are shown in Fig. 2. Fig. 2(A) and (B) show the results for the $\alpha\text{-Fe}_2\text{O}_3$ microcubes with an average size of 300 nm on the edges, which is much larger than the crystal size obtained from X-ray line broadening (38 nm). However, the size repartition was not monodispersed, and a few smaller-sized cubes were observed in Fig. 2(B). Moreover, as shown in Fig. 2(A) and (B), the surfaces of the cubes were rough, which indicated that the cubes were aggregated nanoparticles. Fig. 2(C) and (D) show the TEM images of the $\alpha\text{-Fe}_2\text{O}_3\text{-S}$, which exhibited a spherical morphology with an average diameter of approximately 150 nm. Although the average diameter of

Table 1Physico-chemical properties of different morphologies of α - Fe_2O_3 precursors and Fe_3O_4 .

| Sample | Morphology | α - Fe_2O_3 | | Fe_3O_4 | | | |
|------------------------------|------------|---|-------------|---------------------------------------|--|--|-------------|
| | | SSA ^a /(m ² g ⁻¹) | D^b /(nm) | SSA/(m ² g ⁻¹) | Total Fe ^{II} /Fe ^{III} ratio ^c | Surface Fe ^{II} /Fe ^{III} ratio ^d | D^b /(nm) |
| Fe_xO_y -C | Microcube | 3.4 | 38 | 2.8 | 0.49 ± 0.2 | – | 65 |
| Fe_xO_y -S | Nanosphere | 12.3 | 34 | 10.9 | 0.53 ± 0.2 | – | 42 |
| Fe_xO_y -R | Nanorods | 46.5 | 24 | 24.7 | 0.56 ± 0.2 | 0.53 ± 0.2 | 37 |
| Fe_xO_y -Com | Uniform | 0.4 | 49 | 0.5 | 0.32 ± 0.2 | 0.25 ± 0.2 | 79 |

^a SSA is the specific surface area evaluated using the BET model.^b D is the crystal domain size evaluated from the X-ray line broadening using the Scherrer equation.^c Bulk ratio between Fe^{II} and Fe^{III} in Fe_3O_4 (molar ratio of Fe²⁺ and Fe³⁺ in the Fe_3O_4 content).^d Surface ratio of Fe^{II} and Fe^{III} obtained by XPS analysis.

Fe_2O_3 -S was significantly larger than the particle based on XRD analysis, the high-magnification TEM images (Fig. 2(D)) indicated that the nanospheres were composed of individual nanoparticles with an average size of approximately 30–40 nm, which was consistent with the results calculated from the Scherrer formula. Finally, Fig. 2(E) and (F) present typical TEM images of the α - Fe_2O_3 with nanorod morphology (Fe_2O_3 -R) obtained through the hydrothermal treatment in alkaline media of an iron chloride precursor and a $\text{C}_{10}\text{mimCl}$ additive, but with a NaOH concentration greater than that used to prepare the Fe_2O_3 -C samples. Fig. 2(E) and (F) show that the nanorods exhibited diameters in the range of 20–60 nm and lengths of 200–600 nm. However, pores broad in size and not regular were visible by TEM, at the outer surface within the annealed Fe_2O_3 -R nanoparticles. Unfortunately, N_2 physisorption was not appropriate to determine a mean pore size in this material, due to the very wide repartition in size of the pores. Such intra-rod porosity was probably at the origin of the high surface area observed for this material (Table 1).

3.1.4. TPR results for Fe_2O_3 -R and the commercial material

The reduction behaviors of hematite type materials were examined using TPR under H_2 . Results obtained for Fe_2O_3 -R and Fe_2O_3 -Com are shown in Fig. 3. The experimental TPR profile of α - Fe_2O_3 exhibited two well-resolved reduction peaks, located at 400 °C and 700 °C. Comparable reduction profiles were obtained for the Fe_2O_3 -C and Fe_2O_3 -S materials, showing that crystal size and aggregate morphology do not strongly impact the reduction process. The first reduction process occurred in the temperature range of 300–420 °C with a peak centered at 400 °C. As suggested by the XRD analyses and by previous works [30], the results for the sample obtained via a TPR experiment interrupted at 400 °C and the sample quenched to room temperature indicated that this reduction was related to the presence of α - Fe_2O_3 that was reduced to FeO at 400 °C, with the formation of Fe_3O_4 phase as intermediate product of reduction [45]:

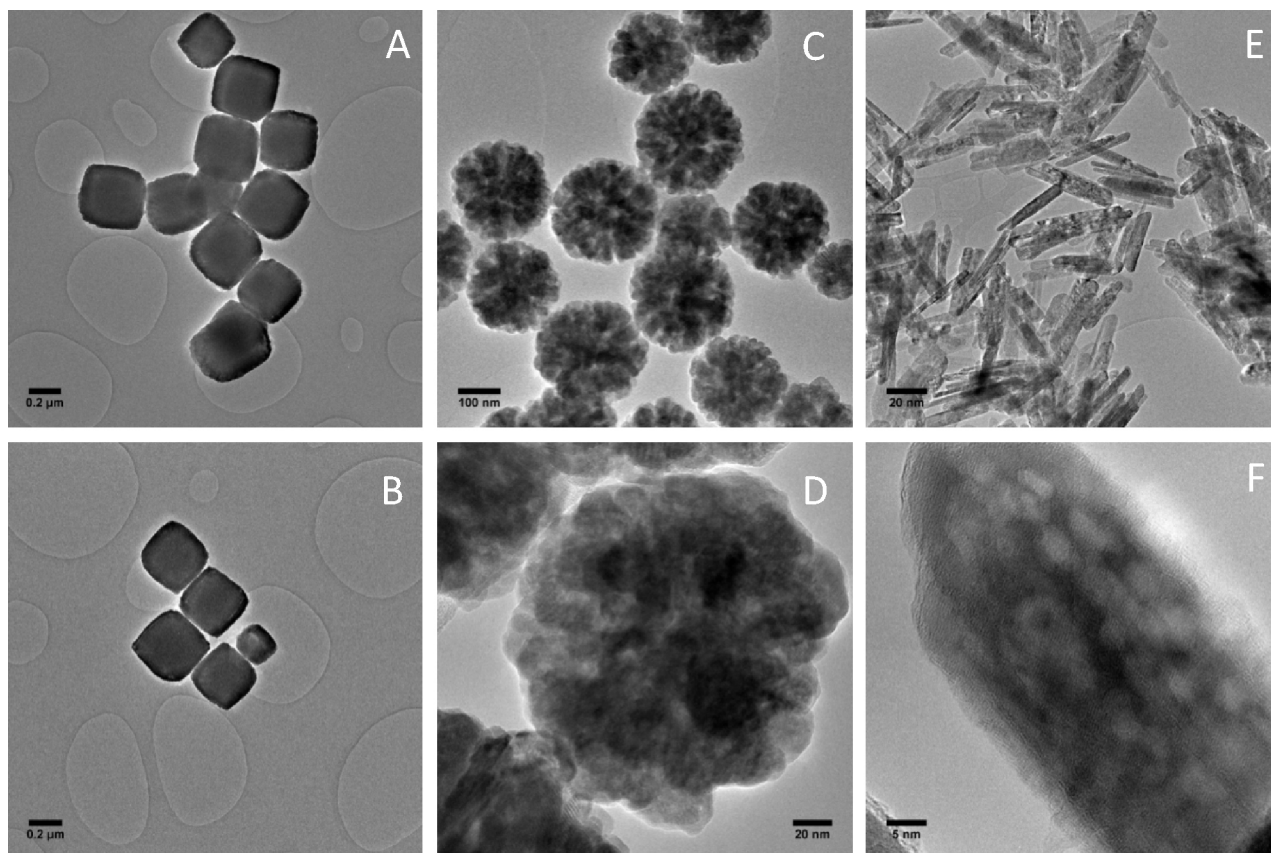


Fig. 2. Representative high magnification TEM images of the different morphologies of α - Fe_2O_3 precursor: (A) and (B): Fe_2O_3 -C; (C) and (D): Fe_2O_3 -S; (E) and (F): Fe_2O_3 -R.

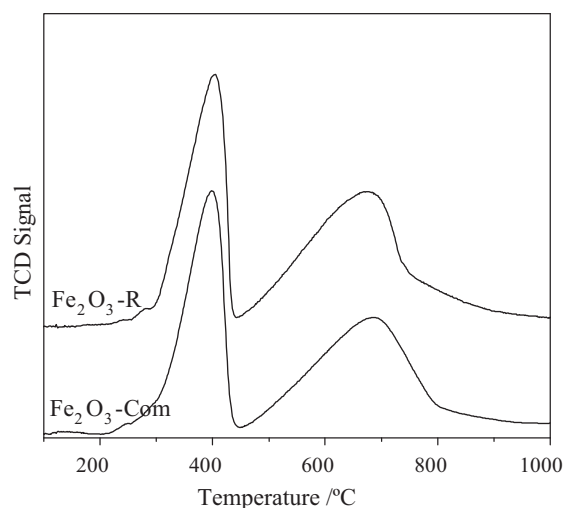


Fig. 3. TPR-H₂ profiles recorded for α-Fe₂O₃ precursor (Fe₂O₃-Com, Fe₂O₃-R).

At temperatures greater than 450 °C, another reduction process was observed (Fig. 3). The peaks with maxima located near 700 °C were due to the second reduction step from FeO to metallic iron:



Given that the total experimental H₂ consumption was lower than the theoretical H₂ consumed for complete reduction of Fe³⁺ to Fe⁰, the Fe³⁺ reduction in the first stage could be assigned to Fe₂O₃ → FeO with 100% of the Fe³⁺ participating in this reduction step, while the second reduction step consists in the incomplete reduction of FeO to Fe⁰ (Table 2). For comparison, the reduction behavior of commercial α-Fe₂O₃ was also investigated. For the Fe₂O₃-Com sample, reduction peaks centered at 405 °C and 685 °C were observed. A comparison of the reduction behavior of Fe₂O₃-Com with that of Fe₂O₃-R revealed that the reduction of Fe₂O₃-R led to a slightly increased total H₂ consumption, and 16.1 mmol g⁻¹ H₂ was consumed (Table 2). Furthermore, the Fe²⁺ reduction at the second stage could be considered as FeO → Fe⁰, and 78.9% of the Fe²⁺ participated in this reduction for Fe₂O₃-R. For comparison, 67.2% of Fe²⁺ was reduced to Fe⁰ in Fe₂O₃-Com. Such an improvement in iron reducibility in Fe₂O₃-R was attributed to the adequate physicochemical properties, which included a significantly greater surface area, a smaller crystal size and the suppression of crystal agglomeration that are all in favor of an increased reducibility.

3.2. Characterization of different morphologies of Fe₃O₄ nanostructures

3.2.1. X-ray diffraction results

Fe₃O₄ phases were obtained through the reduction of the α-Fe₂O₃ [37]. Conditions applied were reduction under H₂ at 300 °C for 1 h. The XRD patterns in Fig. 4 reveal that all of the diffraction peaks of the three powders could be unambiguously assigned to the pure face-centered cubic structure of Fe₃O₄ magnetite (JCPDS Card 19-0629). The diffraction peaks located at 2θ = 30.2, 35.6, 43.2, 53.6, 57.1, 62.6, and 74.2° could be indexed to the (2 2 0), (3 1 1), (4 0 0), (4 2 2), (5 1 1), (4 4 0), and (5 5 3) planes of Fe₃O₄, respectively, by comparison with previously reported data for Fe₃O₄ phase [15,46,47]. As shown in Table 1 and Fig. 4, the difference in the FWHM and in the intensities of the diffraction peaks suggested differences in the crystal sizes and morphologies. Compared to the α-Fe₂O₃, the Fe₃O₄ materials presented larger crystal sizes (Table 1) showing that the phase transformation was accompanied by a sensible crystal growth. The crystal sizes determined from the XRD results using the Scherrer equation were 65, 42, and 37 nm for

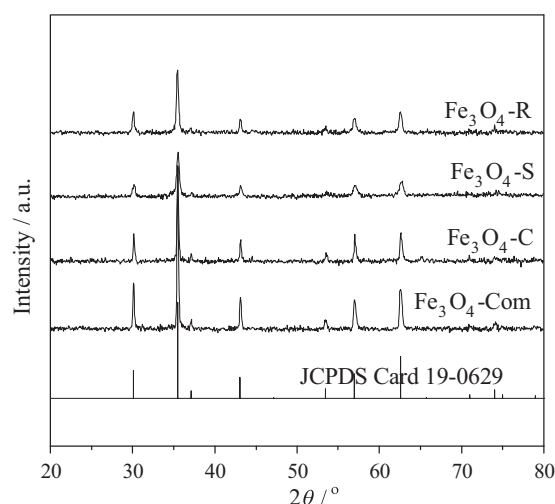


Fig. 4. XRD patterns recorded for different morphologies of Fe₃O₄ (Fe₃O₄-C, Fe₃O₄-S, Fe₃O₄-R).

Fe₃O₄-C, Fe₃O₄-S, and Fe₃O₄-R, respectively. For comparison, the crystal size of the commercial Fe₃O₄ was 79 nm.

3.2.2. Evolution of physical properties

The reducing conversion of the α-Fe₂O₃ into Fe₃O₄ induced some change in textural properties. After reduction, the surface area was relatively smaller than that of the α-Fe₂O₃ precursor. The specific surface areas obtained from N₂ adsorption measurements for the corresponding samples were, 2.8, 10.9, and 24.7 m² g⁻¹, respectively. Notably, the specific surface area of Fe₃O₄-R was larger than that of the other Fe₃O₄ nanoparticles, and this sample exhibited a smaller crystal size than the other samples. In addition, Fe^{II}/Fe^{III} ratios were also measured both in the bulk and on the material surface by chemical analysis (Table 1) and XPS (Figure S1 and Table 1), respectively. It is evident that the same trends of Fe^{II}/Fe^{III} ratio both in the bulk and on the surface were obtained (Table 1). Theoretical Fe^{II}/Fe^{III} ratio is 0.5 for Fe₃O₄ materials. As can be observed in Table 1, ratios obtained over the IL mediated materials were close to this theoretical value. However, lower ratios were obtained for the Fe₃O₄-Com material, despite that a pure magnetite phase was obtained by XRD. As mentioned above, the favorable physical properties of Fe₃O₄-R, such as small crystal size, large surface area, in addition to a high Fe^{II}/Fe^{III} ratio, is suspected to lead to excellent catalytic performances.

3.2.3. Morphology of Fe₃O₄

The morphologies of magnetite catalysts were successfully maintained after thermal transformation of the precursor to Fe₃O₄. The morphology of the Fe₃O₄-C nanoparticles with highly geometrical symmetry was visualized using TEM. The images showed that the average size of the cubes was 350 nm on edge, which was slightly larger than the corresponding size of the Fe₂O₃-C precursor. The TEM images also revealed that the surfaces of the microcubes were relatively rough (Fig. 5(A)), which was further confirmed using high-magnification TEM (Fig. 5(B)). Some pale areas between the dark nanoparticles were observed, which suggests the existence of mesopores inside the microcubes that can be at the origin of the surface area developed by this material. Fig. 5(C) and (D) represent typical TEM images of the Fe₃O₄-S. A spherical morphology, with an average diameter of 200–400 nm, is easily observed. As microcubes, the nanospheres were constructed by the self-assembly of nanoparticles. Finally, a typical TEM image of the Fe₃O₄-R obtained through reduction of the as-prepared Fe₂O₃-R precursor was presented. Fig. 5(E) and (F) show nanorods with

Table 2
H₂-TPR results for α -Fe₂O₃ and Fe₃O₄.

| Samples | Theoretical H ₂ consumption ^a /mmol g ⁻¹ | | | Experimental H ₂ consumption/mmole g ⁻¹ | | | |
|-------------------------------------|---|-------------------------------------|---------------------|---|---|--|------------------------------------|
| | Fe ₂ O ₃ →FeO | Fe ₃ O ₄ →FeO | FeO→Fe ⁰ | Total ^b | Fe ₂ O ₃ →FeO percentage ^c (%) | Fe ₃ O ₄ →FeO percentage (%) | FeO→Fe ⁰ percentage (%) |
| Fe ₂ O ₃ -Com | 6.3 | – | 12.5 | 14.7 | 100.0 | – | 67.2 |
| Fe ₂ O ₃ -R | – | – | – | 16.1 | 100.0 | – | 78.9 |
| Fe ₃ O ₄ -Com | – | 4.3 | 12.9 | 10.9 | – | 100.0 | 51.3 |
| Fe ₃ O ₄ -R | – | – | – | 13.4 | – | 100.0 | 70.0 |

^a Calculated values of H₂ to be consumed for the complete reduction of the cations (reduction reactions considered depicted in the table).

^b Total molar of H₂ consumed for per gram of materials, issued from H₂-TPR experiment.

^c Reduction proportion calculated by comparing each experimental H₂ consumptions with theoretical H₂ consumption.

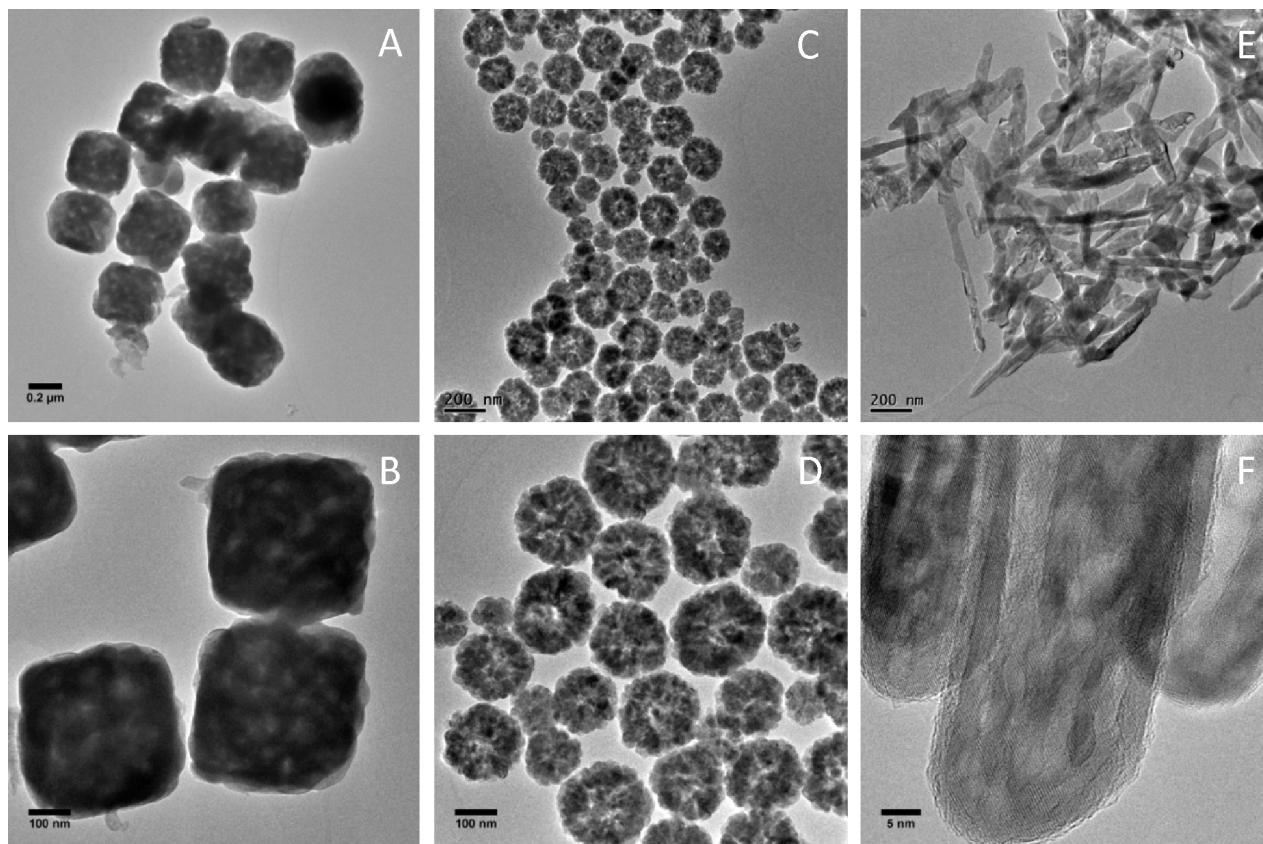


Fig. 5. Representative high magnification TEM images of the different morphologies of Fe₃O₄: (A) and (B): Fe₃O₄-A; (C) and (D): Fe₃O₄-C; (E) and (F): Fe₃O₄-R.

diameters in the range of 40 to 80 nm and lengths from 200 to 600 nm. A high-magnification TEM image of the tip portion of a nanorod showed clear fringes (Fig. 5(F)). As observed on the Fe₂O₃-R precursor, pores of irregular shape and broad in size are clearly observed by TEM.

3.2.4. TPR results of Fe₃O₄-R and Fe₃O₄-Com

Fig. 6 shows the TPR results of Fe₃O₄-R and Fe₃O₄-Com in the temperature range of 50–1000 °C. As in the case of the reduction of the hematite materials, similar reduction profiles were obtained over the Fe₃O₄-C and Fe₃O₄-S materials. Two reduction peaks are observed. H₂ consumptions at each step were calculated; the results are listed in Table 2. The reduction at the first stage (maximal consumption at 400–450 °C) was assigned to the Fe₃O₄ to FeO transition, with 100% of Fe³⁺ present in Fe₃O₄ reducing at this step into Fe²⁺ (Table 2). When the temperature was greater than 500 °C, the second reduction process was observed (Fig. 6). This reduction step (maximal consumption at 700–750 °C) was attributed to the reduction FeO→Fe⁰. However, only a limited fraction of Fe²⁺ participated in this second reduction process. The total H₂ consumption

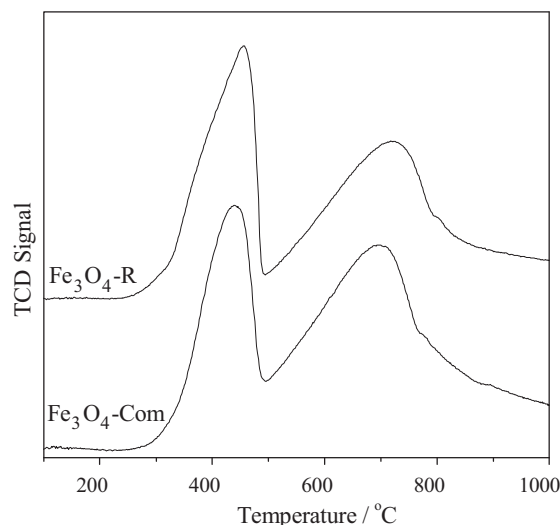


Fig. 6. TPR-H₂ profiles recorded for Fe₃O₄ (Fe₃O₄-Com, Fe₃O₄-R).

Table 3Selected reaction results and catalyst stability for the phenol degradation. (Fe_3O_4 : 0.25 g L^{-1} ; phenol initial concentration: 600 mg L^{-1} ; H_2O_2 : 40 mmol L^{-1} , pH: 4.0, T : 25°C).

| Sample | $C_0^a/\text{mg L}^{-1}$ | $X_{\text{phenol}}^b/\%$ | $X_{\text{TOC}}^c/\%$ ($X_{\text{H}_2\text{O}_2}^d/\%$) | Fe_{tot}^f leaching ^f / mg L^{-1} | Fe_{tot} in solution ^g /% |
|---|--------------------------|--------------------------|---|---|--|
| Homogenous with 0.2 mg L^{-1} of Fe^{2+} | 587 | 32.1 | 27.3 | – | – |
| $\text{Fe}_3\text{O}_4\text{-C}$ | 576 | 67.1 | 38.4 (82.3) | 0.03 | 0.01 |
| $\text{Fe}_3\text{O}_4\text{-S}$ | 405 | 93.2 | 52.4 (83.2) | 0.50 | 0.20 |
| $\text{Fe}_3\text{O}_4\text{-R-1}^e$ | 304 | 98.0 | 74.0 (87.3) | 0.17 | 0.07 |
| $\text{Fe}_3\text{O}_4\text{-R-2}^e$ | | 97.1 | 72.3 | 0.14 | 0.06 |
| $\text{Fe}_3\text{O}_4\text{-R-3}^e$ | | 92.9 | 67.9 | 0.15 | 0.06 |
| $\text{Fe}_3\text{O}_4\text{-Com}$ | 598 | 54.7 | 32.1 (72.5) | 0.27 | 0.11 |

^a C_0 is the phenol concentration, after adsorption on the catalyst surface.^b X_{phenol} is the phenol conversion after 90 min of reaction.^c X_{TOC} is the TOC abatement after 90 min of reaction.^d $X_{\text{H}_2\text{O}_2}$ is the hydrogen peroxide conversion.^e $\text{Fe}_3\text{O}_4\text{-R-1}$, $\text{Fe}_3\text{O}_4\text{-R-2}$ and $\text{Fe}_3\text{O}_4\text{-R-3}$ are the catalysts used for one, two and three successive tests.^f Fe_{tot} leaching in solution is the total iron content in the solution at the end of the reaction.^g Fe_{tot} leaching (%) is the percentage of total iron (Fe^{II} and Fe^{III}) leached from the catalyst at the end of the reaction.

measured for $\text{Fe}_3\text{O}_4\text{-R}$ indicates that only 70.0% of Fe^{2+} reduced to Fe^0 , which was however greater than the reduction degree in the commercial material (51.3%) (Table 2). This result shows that the improved reducibility of iron in nanorod morphology was maintained even in the Fe_3O_4 structure that is not surprising since the intermediate reduction step was performed at relatively low temperature (e.g. 300°C).

3.3. Comparison of the catalytic activity of different iron oxide nanoparticles

Magnetite (Fe_3O_4) and hematite ($\alpha\text{-Fe}_2\text{O}_3$) were used to investigate the effect of surface ferrous species (Fe^{II}) on iron oxide during Fenton-like reactions. In our study, $\text{Fe}_2\text{O}_3\text{-R}$ and $\text{Fe}_3\text{O}_4\text{-R}$ were used because of their high surface areas, small crystal sizes, and porous structures. Phenol conversion and TOC abatement curves obtained for $\text{Fe}_2\text{O}_3\text{-R}$ and $\text{Fe}_3\text{O}_4\text{-R}$ were presented in Fig. 7. Almost no conversion of phenol was observed (5.7%), and only 4.0% TOC was removed, using $\text{Fe}_2\text{O}_3\text{-R}$ as catalyst. However, iron oxides containing mainly surface ferric species (Fe^{III}), e.g. $\alpha\text{-Fe}_2\text{O}_3$, are known to be nearly inactive for H_2O_2 decomposition into active radicals [30]. Consequently, this material leads to very limited phenol conversion. The concentration of H_2O_2 was measured at the end of the $\text{Fe}_2\text{O}_3\text{-R}/\text{H}_2\text{O}_2$ reaction. A H_2O_2 concentration of 4.3 mmol L^{-1} was obtained despite the very limited phenol conversion. This result shows that H_2O_2 adsorbs rather than decomposes on the surface of

$\text{Fe}_2\text{O}_3\text{-R}$. It agrees with the observation that the adsorption of H_2O_2 onto Fe^{III} sites (Eq. (5)) was faster than the adsorption of organic molecules [48].



Compared with $\text{Fe}_2\text{O}_3\text{-R}$, $\text{Fe}_3\text{O}_4\text{-R}$ showed a much greater removal efficiency of phenol, with almost complete conversion after 90 min, while the TOC abatement was 74.0%. These results clearly indicated that Fe^{II} surface sites played an important role in the activation of the H_2O_2 molecule. Moreover, the $\text{Fe}_3\text{O}_4\text{-R}$ catalyst could be conveniently separated from the reaction mixture through the application of an external magnetic field. In the case of reaction with $\text{Fe}_3\text{O}_4\text{-R}$ (Table 3), the conversion of H_2O_2 was 87.3% at the end of the reaction that is consistent with the high phenol conversion and high TOC abatement obtained.

3.4. Evidence of heterogeneous Fenton reaction over $\text{Fe}_3\text{O}_4\text{-R}$

An evaluation of the catalytic activity in the degradation of phenol by $\text{Fe}_3\text{O}_4\text{-R}$ was performed under different experimental conditions (Fig. 8(A) and (B)). The results showed that phenol conversion was limited with hydrogen peroxide alone (33.0%), with a TOC abatement of 25.3%. When the catalyst was added to the phenol solution, 45.1% of the TOC was removed. When we separated the catalyst, and added the new phenol solution (600 mg L^{-1}) to the catalyst for another 90 min, no more than 10.0% phenol disappear with less than 5.0% TOC abatement in the second run, which shows that the observed removal of phenol can be attributed to material surface adsorption (SI, Figure S2). It is probably due to the porous structure and high surface area of $\text{Fe}_3\text{O}_4\text{-R}$, which is in favor of phenol adsorption. Furthermore, the phenol removal efficiency of the heterogeneous catalytic system is highlighted in Fig. 8, and as we previously mentioned, high phenol conversion and TOC abatement were obtained in the $\text{Fe}_3\text{O}_4\text{-R}/\text{H}_2\text{O}_2$ process.

The high activity of Fe_3O_4 is obviously related to the capability of the material surface to convert H_2O_2 molecules into free radicals ($\cdot\text{OH}$) [48]. Under acidic conditions, the mechanism of H_2O_2 decomposition over Fe_3O_4 may involve adsorption on Fe^{2+} and Fe^{3+} surface sites. Adsorption and formation of a complex between surface Fe^{III} site and H_2O_2 (Eq. (6)) can occur, allowing the production of $\cdot\text{HO}_2$ radical that can thereafter react to form dioxygen (Eq. (7)). However, the rates of radical formation over Fe^{II} are slow [49], compared to the rate of radical production over Fe^{II} surface sites (Eq. (8)) that are responsible for the phenol degradation.

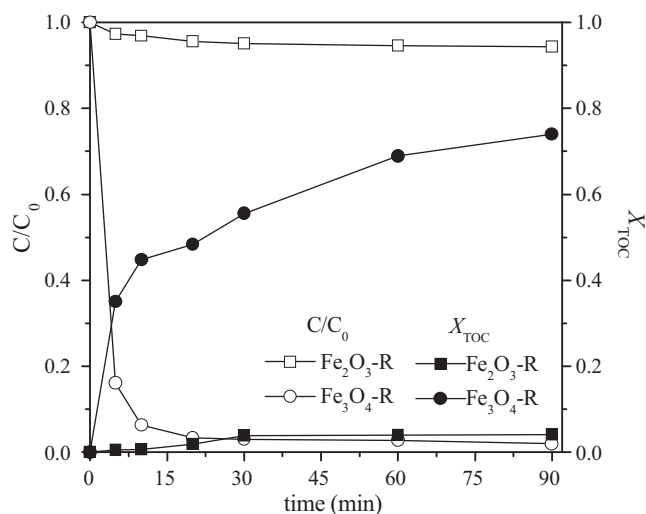


Fig. 7. Degradation and mineralization of phenol over rod-type morphology in the presence of H_2O_2 (phenol initial: 600 mg L^{-1} , $\text{Fe}_2\text{O}_3\text{-R}$: 0.25 g L^{-1} or Fe_3O_4 : 0.25 g L^{-1} , H_2O_2 : 40 mmol L^{-1} , pH: 4.0, T : 25°C).

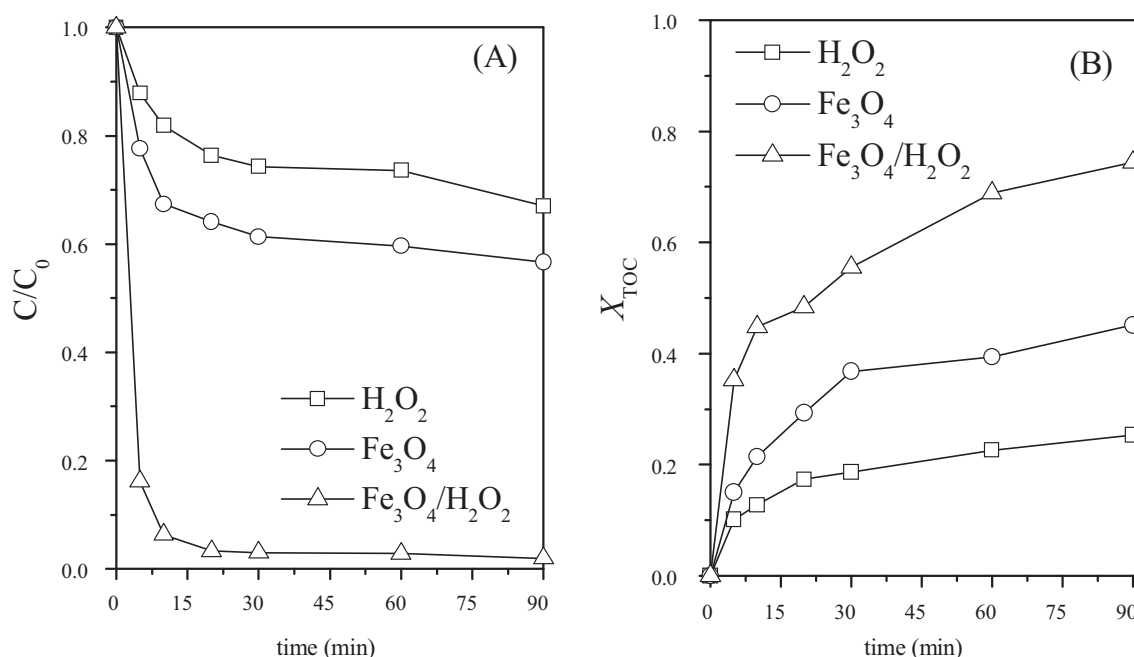


Fig. 8. Phenol removal efficiency (A) and TOC removal efficiency (B) obtained with hydrogen peroxide alone (blank), catalyst alone (adsorption test), and hydrogen peroxide and catalyst (catalytic degradation) (phenol initial: 600 mg L^{-1} , Fe_3O_4 -R: 0.25 g L^{-1} , H_2O_2 : 40 mmol L^{-1} , pH: 4.0, T : 25°C).



Furthermore, formation of soluble Fe^{2+} was also measured during the reaction (Table 3). However, the iron leaching remains at the ppm level in the solution. A blank experiment, performed with a similar content in Fe^{2+} as homogeneous catalyst (Table 3, 0.2 mg L^{-1} in Fe^{2+} experiment), was performed. Limited phenol conversion (32.1%) and TOC abatement (27.3%) was obtained, indicating that the contribution of dissolved iron is limited, especially when we compare these values to the values obtained for the more active materials. Then, the high phenol conversion and TOC abatement measured for the Fe_3O_4 -R can be attributed to reaction over heterogeneous active sites on the material surface.

3.5. Role of morphology in the catalytic oxidation of phenol

Different morphologies exhibited different surface areas, adsorption abilities, and crystal sizes, which are considered to be the decisive parameters that contribute to catalytic performance [50,51]. In our study, different shapes of Fe_3O_4 (Fe_3O_4 -C, Fe_3O_4 -S, or Fe_3O_4 -R, presenting microcubes, nanospheres, and nanorods, respectively) were chosen to estimate the effect of catalyst morphology on the catalytic activity when H_2O_2 was used as an oxidant. The phenol, TOC removal efficiencies, and H_2O_2 conversions obtained at the end of the tests were summarized in Table 3. As evident in Fig. 9 and Table 3, Fe_3O_4 -R exhibited superior catalytic activity in the Fe_3O_4/H_2O_2 process compared with the other morphologies of Fe_3O_4 . Notably, the three different catalysts synthesized here were much more active than the commercial material (Fe_3O_4 -Com), for which only 54.7% of the phenol was converted, 32.1% of the TOC was removed, and 72.5% of the H_2O_2 was consumed. The results in Fig. 9, Table 1, and Table 3 then revealed that a greater surface area was beneficial to the reaction, leading to high phenol mineralization degree. Evolution of the pseudo-first order reaction rate with the surface area was presented in Fig. 10. The activity trend obtained was: Fe_3O_4 -R \gg Fe_3O_4 -S \gg Fe_3O_4 -C $>$ Fe_3O_4 -Com. The results clearly indicated that this process was a surface reaction since increased surface area provided more active sites for

catalytic oxidation, and consequently higher constant rate. Higher content of surface hydroxyl radicals could be produced over high surface area materials, enhancing the degradation of phenol [51]. Consequently, the very limited activity of the catalyst prepared by reduction of the commercial hematite, that is Fe_3O_4 -Com, resulted from its poor textural properties.

Greater Fe^{II}/Fe^{III} ratios led to more Fe^{II} sites and resulted in higher removal efficiency for organic compounds [52]. As evident from the results in Table 1, comparable bulk Fe^{II}/Fe^{III} ratios were obtained between the different morphologies of the synthesized Fe_3O_4 . These were however slightly higher than the ratio measured in the commercial catalyst (0.32 ± 0.2). Therefore, the significantly higher catalytic activities of the synthesized samples mainly originated from the higher surface areas, as demonstrated by Fig. 10, due to the increase in exposed active site number with the surface area at iso- Fe^{II}/Fe^{III} ratios.

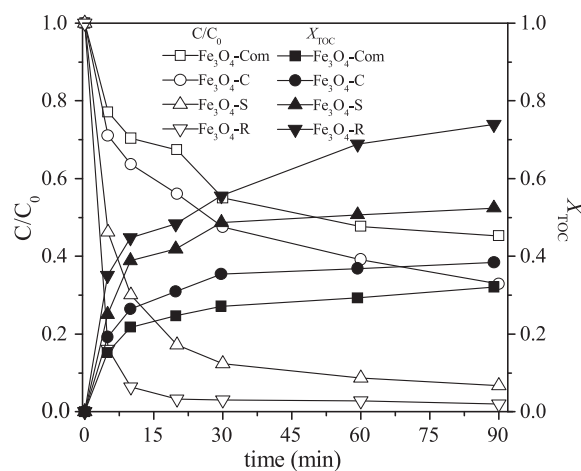


Fig. 9. Phenol removal efficiency and TOC removal obtained with different morphology of Fe_3O_4 (phenol initial: 600 mg L^{-1} , catalysts: 0.25 g L^{-1} , H_2O_2 : 40 mmol L^{-1} , pH: 4.0, T : 25°C).

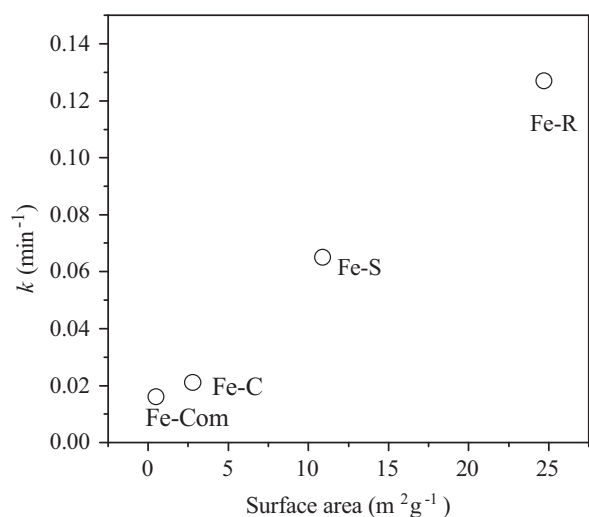


Fig. 10. The relationship between the constant rate and surface area of the different catalysts.

3.6. Influence of hydrogen peroxide concentration and catalyst loading on phenol oxidation

In the heterogeneous Fenton reaction, the concentration of oxidant and catalyst loading are essential to the reaction and directly affect the concentration of active radical produced for phenol degradation. We investigated the effect of hydrogen peroxide concentration by increasing the hydrogen peroxide concentration from 10 mmol L⁻¹ to 50 mmol L⁻¹ (SI, Figure S3). The effect of catalyst loading on phenol conversion and TOC abatement in the Fe₃O₄-R/H₂O₂ system was also evaluated (details seen in SI, Figure S4). TOC abatement increased with increasing H₂O₂ concentration and increasing catalyst loading (SI, Figure S3 and S4).

Logically, the removal efficiency was dependent on H₂O₂ concentration. An increase in H₂O₂ concentration, resulting in increased •OH production, leads to increased phenol conversion and TOC abatement. As evident in Figure S3, the TOC abatement increased with increasing H₂O₂ dosage up to 40 mmol L⁻¹. However, further increase in the concentration of H₂O₂ to 50 mmol L⁻¹ did not induce significant increase in the TOC abatement (82.3%). According to the stoichiometry for the complete phenol degradation by H₂O₂, 14 mol of H₂O₂ is theoretically required to completely convert 1 mol phenol to CO₂ and H₂O. In our study, 10, 20, 30 or 40 mmol L⁻¹ of H₂O₂ was added to 100 mL of phenol solution (at the initial concentration of ~300–305 mg L⁻¹ after adsorption stabilization). These concentrations in H₂O₂ were however below the stoichiometric value needed to completely mineralize phenol (45.3 mmol L⁻¹ of H₂O₂). Consequently, complete phenol conversion and TOC abatement cannot be achieved under these conditions. When H₂O₂ concentration increased to 50 mmol L⁻¹, the H₂O₂/phenol molar ratio was 15.4, which was 1.1 times larger than the stoichiometric value needed to completely mineralize phenol into inorganic compounds (CO₂, H₂O). However, complete TOC abatement could not be obtained even at the highest H₂O₂ value, and TOC abatement of only 82.3% is obtained.

The effect of Fe₃O₄ loading was also given for the sake of information. As can be awaited, an increase in catalyst loading induced an increase in final phenol conversion (Figure S4). The increase in catalyst loading resulted in an increase in Fe^{II} surface active site number that logically results in enhanced final phenol conversion.

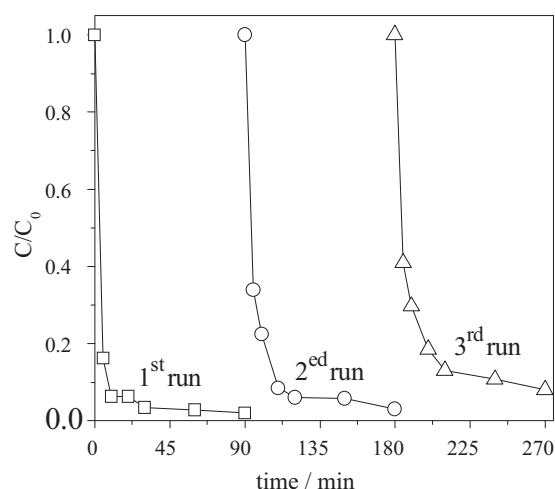


Fig. 11. Evaluation of the catalyst stability during the reaction. (phenol initial: 600 mg L⁻¹, Fe₃O₄-R: 0.25 g L⁻¹, H₂O₂: 40 mmol L⁻¹, T: 25 °C).

3.7. Stability of Fe₃O₄-R catalyst and iron leaching

For the Fe₃O₄/H₂O₂ system, the stability of the catalyst is a critical factor for its successful application to wastewater treatment. The reusability of the solid was consequently evaluated by three successive runs under identical oxidation conditions. At the end of each oxidation process, the solid was removed from the reactor, dried in a quartz tube under N₂ at a flow rate of 60 mL min⁻¹ at 60 °C overnight, and stored at room temperature. As shown in Fig. 11, the removal efficiency slightly decreased after the three cycles. Due to the possible oxidation of the catalyst surface during reaction, XPS was employed to quantify the changes of Fe²⁺/Fe³⁺ ratio (SI file, Table S1, Figure S1). A significant part of the Fe²⁺ was observed to oxidize into Fe³⁺ after reaction (the ratio of Fe²⁺/Fe³⁺ reduced to 41.0%, compared with 52.5% for the fresh material). This evolution could explain the slight decrease in final conversion between the three successive cycles. However, the phenol conversion and TOC abatement still remained high (Table 3), which indicated that satisfying catalytic performance was maintained after three runs even if the Fe₃O₄ was observed to slightly dissolve at each cycle (the total iron ion concentration in solution was 0.14–0.17 mg L⁻¹ at the end of each test, Table 3). The morphology of Fe₃O₄ after the three consecutive uses was comparable to that of the fresh material (SI, Figure S5). In addition, XRD diffractograms collected before and after the oxidation reaction were found to be comparable (SI, Figure S6). Satisfying stability of the structure, and activity maintain under cyclic reaction tests (*i.e.*, limited deactivation of the surface catalytic sites by the adsorption/oxidation process was observed after three successive tests) was thus obtained.

3.8. Effect of the iron crystal phase on the catalytic oxidation of phenol

Different crystal phases contain different amounts of active sites, which is a decisive parameter that contributes to catalytic performance. Therefore, the material phase composition can affect the degradation of phenol during catalytic oxidation. Different iron phases were thus obtained through reduction of the α-Fe₂O₃ under H₂ at 300 °C, 400 °C, and 600 °C for 1 h. The crystalline phases of the catalyst samples were then assessed based on their XRD patterns (Fig. 12). The XRD patterns showed that the iron crystal phase depended on the reduction temperature. The diffraction peaks of Fe₂O₃-R reduced at 300 °C was assigned to Fe₃O₄-R. No additional phases were detected in the samples, which suggested that the

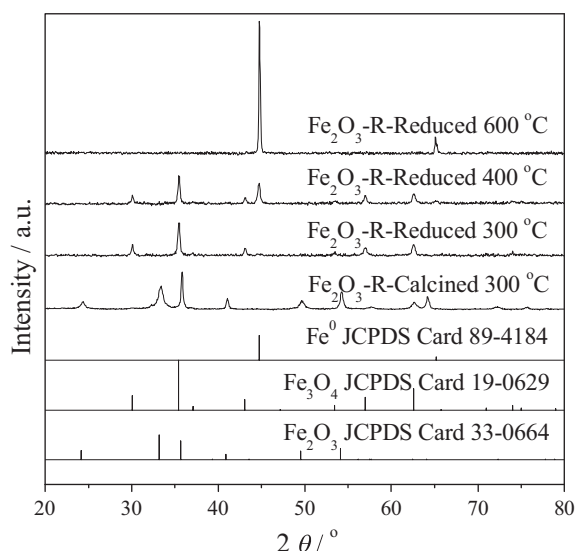


Fig. 12. XRD patterns recorded of α - Fe_2O_3 -R precursor oxidized at 300°C and reduced at different temperatures (300°C , 400°C and 600°C) for 1 h.

Fe_3O_4 -R was pure magnetite. When the reduction temperature was increased to 400°C , the iron mixed phase $\text{Fe}_3\text{O}_4/\text{Fe}^0$ was obtained, which was also reported by Moura et al. [15]. When the reduction temperature was increased to 600°C , the Fe_3O_4 phase vanished completely and was transformed into pure Fe^0 . This result was not in agreement with results obtained by TPR experiments for which incomplete reduction was measured even at 1000°C (Table 2). However, the low H_2 concentration used for the TPR experiments could be at the origin of the incomplete reduction.

To investigate whether the crystal phase of the iron was correlated with the degradation of phenol, samples with different crystal phase combinations were used to compare removal efficiencies. TOC abatement, which is an important parameter for evaluating the mineralization degree of organic compounds, was used to affirm the efficiency of catalytic degradation of phenol with H_2O_2 . The phenol conversion and TOC abatement after 90 min are presented in the Figure S7 (SI file). The final conversion increased with increasing reduction temperature up to 400°C and then decreased when the reduction temperature reached 600°C , showing the variable contribution of the different phases to the apparent activity. Fe^0 exhibited some activity, with 68.1% TOC abatement, even if greater degradation were obtained for Fe_3O_4 -R. The $\text{Fe}_3\text{O}_4/\text{Fe}^0$ phase (reduction at 400°C , Fig. 12) exhibited the highest catalytic activity and TOC removal efficiency (82.0%), and the catalytic activity followed the order $\text{Fe}_3\text{O}_4/\text{Fe}^0 > \text{Fe}_3\text{O}_4 > \text{Fe}^0$. A positive effect on the catalytic activity was observed with the formation of Fe^0 phase over Fe_3O_4 -R surface (SI, Figure S7). The formation of an interface between Fe^0 with Fe_3O_4 , not only by physical contact but also via a surface chemical reaction to form an interfacial FeO phase, could be at the origin of this high activity [15]. Therefore, we can conclude that the formation of mixed $\text{Fe}^0/\text{Fe}^{\text{II}}$ phase was appropriate to generate high activity for heterogeneous Fenton reactions.

4. Conclusions

Magnetite, Fe_3O_4 , with various morphologies has been successfully synthesized through the thermal reduction of α - Fe_2O_3 particles synthesized via a hydrothermal process. TEM analysis indicated that microcubes, nanospheres, and nanorods of the Fe_3O_4 particles were porous structures. The nanorods of Fe_3O_4 exhibited the greatest activity, with a phenol conversion of 98.0% and a TOC

abatement of 74.0%. In addition to the evident effect of the material morphology, studies revealed that the crystal phase was directly responsible for the catalytic degradation through Fe^{II} active site. Stability studies evidenced satisfying stability of these nanomaterials of Fe_3O_4 structure, with limited loss in catalytic activity. In addition, the optimization of the reduction temperature to form $\text{Fe}^0/\text{Fe}_3\text{O}_4$ mixed phase allowed achieving improved catalytic activity. These heterogeneous catalytic processes may be regarded as promising hydroxyl-radical-based systems for the oxidative degradation of organic compounds.

Acknowledgements

This work was supported by the National Natural Science Foundation of China (Grant No. 20977069). Liwei Hou greatly acknowledges the Chinese Science Council for two-year research grant (No. 2010008112) at the University of Poitiers, France. We appreciate the financial support by the Fundamental Research Funds for the Central Universities, China (Grant No. 20102050201000053) and Natural Science Foundation of China (Grant No. 20977069). Sébastien Royer acknowledges the CNRS for attribution of six months delegation.

Appendix A. Supplementary data

Supplementary data associated with this article can be found, in the online version, at <http://dx.doi.org/10.1016/j.apcatb.2013.07.072>.

References

- [1] R.M. Cornell, U. Schwertmann, *The Iron Oxides: Structure, Properties, Reactions, Occurrences and Uses*, 2nd ed., Wiley-VCH, Weinheim, 2004.
- [2] F.B. Li, X.Z. Li, X.M. Li, T.X. Liu, J. Dong, *J. Colloid Interface Sci.* 311 (2007) 481–490.
- [3] G. Kreysa, B. Håkansson, *J. Electroanal. Chem.* 201 (1986) 61–83.
- [4] K.E. Heusler, *Electrochim. Acta* 30 (1985) 1741–1742.
- [5] C.L. Chien, *Annu. Rev. Mater. Sci.* 25 (1995) 129–160.
- [6] U. Preuß, M. Baerns, *Chem. Eng. Technol.* 10 (1987) 297–305.
- [7] L.C.A. Oliveira, J.D. Fabris, R.R.V.A. Rios, W.N. Mussel, R.M. Lago, *Appl. Catal. A: Gen.* 259 (2004) 253–259.
- [8] L.J. Xu, J.L. Wang, *Appl. Catal. B: Environ.* 123–124 (2012) 117–126.
- [9] X.F. Xue, K. Hanna, M. Abdelmoula, N.S. Deng, *Appl. Catal. B: Environ.* 89 (2009) 432–440.
- [10] W.P. Kwan, B.M. Voelker, *Environ. Sci. Technol.* 37 (2003) 1150–1158.
- [11] P.G. Tratnyek, M.M. Scherer, T.J. Johnson, L.J. Matheson, *Permeable reactive barriers of iron and other zero-valent metals*, in: M.A. Tarr (Ed.), *Chemical Degradation Methods for Wastes and Pollutants: Environmental and Industrial Applications*, Marcel Dekker, New York, 2003, pp. 371–421.
- [12] J.E. Szecsody, J.S. Fruchter, M.D. Williams, V.R. Vermeul, D. Sklarew, *Environ. Sci. Technol.* 38 (2004) 4656–4663.
- [13] S.H. Joo, A.J. Feitz, T.D. Waite, *Environ. Sci. Technol.* 38 (2004) 2242–2247.
- [14] N. Wang, L.H. Zhu, D.L. Wang, M.Q. Wang, Z.F. Lin, H.Q. Tang, *Ultrason. Sonochem.* 17 (2010) 526–533.
- [15] F.C.C. Moura, M.H. Araujo, R.C.C. Costa, J.D. Fabris, J.D. Ardisson, W.A.A. Macedo, R.M. Lago, *Chemosphere* 60 (2005) 1118–1123.
- [16] P.G. Tratnyek, M.M. Scherer, B. Deng, S. Hu, *Water Res.* 35 (2001) 4435–4443.
- [17] T. Hyeon, S.S. Lee, J. Park, Y. Chung, H.B. Na, *J. Am. Chem. Soc.* 123 (2001) 12798–12801.
- [18] S.H. Yu, M. Yoshimura, *Adv. Funct. Mater.* 12 (2002) 9–15.
- [19] K. Woo, H.J. Lee, J.P. Ahn, Y.S. Park, *Adv. Mater.* 15 (2003) 1761–1764.
- [20] X.W. Teng, H. Yang, *J. Mater. Chem.* 14 (2004) 774–779.
- [21] J.H. Deng, X.H. Wen, Q.N. Wang, *Mater. Res. Bull.* 47 (2012) 3369–3376.
- [22] R.X. Huang, Z.Q. Fang, X.M. Yan, W. Cheng, *Chem. Eng. J.* 197 (2012) 242–249.
- [23] S. Shin, H. Yoon, J. Jang, *Catal. Commun.* 10 (2008) 178–182.
- [24] S.X. Zhang, X.L. Zhao, H.Y. Niu, Y.L. Shi, Y.Q. Cai, G.B. Jiang, *J. Hazard. Mater.* 167 (2009) 560–566.
- [25] S.P. Sun, A.T. Lemley, *J. Mol. Catal. A: Chem.* 349 (2011) 71–79.
- [26] J.B. Zhang, J. Zhuang, L.Z. Gao, Y. Zhang, N. Gu, J. Feng, D.L. Yang, J.D. Zhu, X.Y. Yan, *Chemosphere* 73 (2008) 1524–1528.
- [27] X.F. Xue, K. Hanna, N.S. Deng, *J. Hazard. Mater.* 166 (2009) 407–414.
- [28] K. Rusevova, F.D. Kopinke, A. Georgi, *J. Hazard. Mater.* 241–242 (2012) 433–440.
- [29] M. Usman, P. Faure, C. Ruby, K. Hanna, *Appl. Catal. B: Environ.* 117–118 (2012) 10–17.

- [30] R.C.C. Costa, F.C.C. Moura, J.D. Ardisson, J.D. Fabris, R.M. Lago, *Appl. Catal. B: Environ.* 83 (2008) 131–139.
- [31] L.J. Xu, J.L. Wang, *Environ. Sci. Technol.* 46 (2012) 10145–10153.
- [32] Y.L. Nie, C. Hu, L. Zhou, J.H. Qu, *Appl. Catal. B: Environ.* 82 (2008) 151–156.
- [33] A. Prakash, A.V. McCormick, R.M. Zachariah, *Chem. Mater.* 16 (2004) 1466–1471.
- [34] S. Peng, C. Wang, J. Xie, S.H. Sun, *J. Am. Chem. Soc.* 128 (2006) 10676–10677.
- [35] D.E. Zhang, X.J. Zhang, X.M. Ni, J.M. Song, H.G. Zheng, *Cryst. Growth Des.* 7 (2007) 2117–2119.
- [36] Z. Li, B. Tan, M. Allix, A.I. Cooper, M.J. Rosseinsky, *Small* 4 (2008) 231–239.
- [37] A.P. Alivisatos, *J. Phys. Chem.* 100 (1996) 13226–13239.
- [38] J. Chen, F.B. Wang, K.L. Huang, Y.N. Liu, S.Q. Liu, *J. Alloys. Compd.* 475 (2009) 898–902.
- [39] N. Du, Y.F. Xu, H. Zhang, C.X. Zhai, D.R. Yang, *Nanoscale Res. Lett.* 5 (2010) 1295–1300.
- [40] S.F. Zhang, W. Wu, X.H. Xiao, J. Zhou, F. Ren, C.Z. Jiang, *Nanoscale Res. Lett.* 6 (2011) 89–97.
- [41] J. Bachmann, J. Jing, M. Knez, S. Barth, H. Shen, S. Mathur, U. Gösele, K. Nielsch, *J. Am. Chem. Soc.* 129 (2007) 9554–9555.
- [42] Y.L. Chueh, M.W. Lai, J.Q. Liang, L.J. Chou, Z.L. Wang, *Adv. Funct. Mater.* 16 (2006) 2243–2251.
- [43] L.W. Hou, Q.H. Zhang, F. Jérôme, D. Duprez, F. Can, X. Courtois, H. Zhang, S. Royer, *ChemCatChem* 5 (2013) 1978–1988.
- [44] A.E. Harvey, J.A. Smart, E.S. Arms, *Anal. Chem.* 27 (1955) 26–29.
- [45] M.S. Liang, W.K. Kang, K.C. Xie, *J. Nat. Gas Chem.* 18 (2009) 110–113.
- [46] H. Iida, K. Takayanagi, T. Nakanishi, T. Osaka, *J. Colloid Interface Sci.* 314 (2007) 274–280.
- [47] H. Yan, J. Zhang, C. You, Z. Song, B. Yu, Y. Shen, *Mater. Chem. Phys.* 113 (2009) 46–52.
- [48] M.A. Voinov, J.O. Sosa Pagán, E. Morrison, T.I. Smirnova, A.I. Smirnov, *J. Am. Chem. Soc.* 133 (2011) 35–41.
- [49] S.-S. Lin, M.D. Gurol, *Environ. Sci. Technol.* 32 (1998) 1417–1423.
- [50] T.L.P. Dantas, V.P. Mendonça, H.J. José, A.E. Rodrigues, R.F.P.M. Moreira, *Chem. Eng. J.* 118 (2006) 77–82.
- [51] S. Song, Z.W. Liu, Z. He, A.L. Zhang, J.M. Chen, *Environ. Sci. Technol.* 44 (2010) 3913–3918.
- [52] P.K. Stoimenov, V. Zaikovski, K.J. Klabunde, *J. Am. Chem. Soc.* 125 (2003) 12907–12913.